

Received September 29, 2020, accepted October 17, 2020, date of publication October 26, 2020,  
date of current version November 10, 2020.

Digital Object Identifier 10.1109/ACCESS.2020.3033969

# The Effects of Spectral X-Ray Photon Counting Detector Parameters on Detector Performance: Thickness and Pitch

OLIVER LEN PAUL PICKFORD SCIENTI<sup>1</sup>, (Member, IEEE),

JEFFREY C. BAMBER<sup>2</sup>, (Member, IEEE), AND

DIMITRA G. DARAMBARA<sup>3</sup>, (Member, IEEE)

Joint Department of Physics, The Institute of Cancer Research and The Royal Marsden NHS Foundation Trust, London SM2 5NG, U.K.

Corresponding author: Oliver Len Paul Pickford Scienti (olie.scienti@icr.ac.uk)

This work was supported in part by the Cancer Research U.K. Non-Clinical Centre, Institute of Cancer Research, under Grant C209/A20926, in part by the Cancer Research U.K. Imaging Centre, Institute of Cancer Research (ICR), under Grant C1060/A16464, and in part by the National Health Service (NHS) Funding to the National Institute for Health Research (NIHR) Biomedical Research Centre at the Royal Marsden and ICR.

**ABSTRACT** The design of photon counting spectral imaging (x-CSI) x-ray detectors involves optimising many parameters including pixel thickness, pitch, and type of charge sharing correction algorithm (CSCA) employed, if any. The optimal value for one parameter depends on the other parameter values, as well as extrinsic variables such as application specific photon fluxes and energies of interest. No analytical approaches currently exist for optimising these parameters simultaneously. This work thus utilised our inhouse simulation framework, combining Monte Carlo and finite element methods to systematically simulate the response of 715 different CdTe based x-CSI detectors, comprising 13 different CSCAs, 5 different pixel thicknesses (1 mm – 3 mm), and 11 different pixel pitches (100  $\mu\text{m}$  – 600  $\mu\text{m}$ ). Detector response to monoenergetic irradiation at 80 keV at 4 different fluxes was assessed using a range of metrics. Due to its complexity, the analysis of this work is divided into several publications, with this one focusing on the effects of pixel pitch and thickness. We were able to identify, and provide mechanistic explanations for, general trends in detector performance with varying pixel geometry that will be of interest to x-CSI detectors designers. Superficially similar spectral metrics were found to vary significantly in their sensitivity to different charge sharing mechanisms, underlining the importance of carefully selecting the evaluation metric for photon counting detectors based on their application. The parameters used here were selected based on our own interests, however this work demonstrates the utility of this framework for optimising x-CSI detector parameters for various spectral applications.

**INDEX TERMS** Charge sharing correction, finite element method, hybrid pixelated detector, Monte Carlo, photon counting, spectral x-ray imaging, x-CSI, x-ray detector.

## I. INTRODUCTION

Traditional x-ray imaging technologies make use of energy integrating (EI) approaches, whereby the signal output from a given pixel is the integral of charge in the circuit over some time interval,  $t$ . The charge integrated in pixels in such a detector will be a linear combination of charge generated from photon interactions with the sensor (either directly to electrical charge in the case of semi-conductors or via an

optical photon intermediary in scintillator detectors) and the electronic noise in the circuit. In order to minimise the contribution of the electronic noise to the output signal, the time interval  $t$  is set to be long enough that many photons will deposit their energy in the pixel during the process of charge integration, and so the fractional charge due to electronic noise is minimised. This approach has three related drawbacks:

1). By integrating the charge produced by several different photons into a single signal, EI detectors lose potentially diagnostically useful information regarding how x-ray attenuation

The associate editor coordinating the review of this manuscript and approving it for publication was Aamir Younis Raja<sup>4</sup>.

varies as a function of photon energy. Dual energy detectors compensate for this to some extent by assessing how x-ray spectra with high and low mean energies are differentially attenuated, improving soft tissue contrast. These detectors still use spectra with significant spectral overlap as standard however [1], so involve a higher radiation dose than would be needed if the energy dependent attenuation could be assessed directly.

2). Due to the sensitivity of the detector to total energy deposition, higher energy photons contribute more information to signal formation than lower energy photons. This is of particular detriment in medical imaging applications concerning soft tissue discrimination, where it is the lower energy photons that carry most of the diagnostically relevant information.

3). As electronic noise is integrated in with x-ray induced charge, where the rate of incident photons is particularly low (due to the thickness of patient material or the presence of particularly strongly attenuating material in the path of the x-ray beam such as metal implants) photon starvation can occur, resulting in a much higher contribution of the noise to the generated signal. Images reconstructed from such data will show artefacts including noisy regions. To reduce the effect of electronic noise in reconstructed images EI detectors can use higher fluxes (and consequent higher doses), or larger pixels so as to increase the ratio of x-ray induced charge to electronic noise on a per pixel basis.

EI approaches have been developed which seek to mitigate these drawbacks to various degrees [2], however it is widely expected that the next major step in x-ray detector design will not come from mitigating these disadvantages on an EI detector, but rather from a transition away from EI and towards photon counting (PC).

PC detectors work by attempting to measure the energy of each incoming photon and counting the number of photons that are within a given energy window [3]. Fig. 1 shows how this can be implemented. The intensity of the electronic noise is variable with time, however it is significantly lower than the transient rise in signal produced by the interaction of an x-ray photon with the sensor material. By selecting an energy threshold that is just higher than the electronic noise and applying a counter which records the number of times that the signal rises above the detection threshold, the number of photons interacting with the sensor can be recorded, whilst counts originating solely from electronic noise are effectively excluded from the output. x-ray PC detectors are thus often said to be ‘noise free’ [4] as they register no counts if not irradiated, though electronic noise is of course still present pre-thresholding. Electronic noise may still affect the readout in other ways however, as the recorded counts are superimposed on the noise, which can result in shifts in registered event energies. For the energies relevant to medical imaging however, these shifts in registered energy are often negligible compared with the energy of the incoming photons. Introduction of additional energy thresholds then allows for energy discrimination between detected photons. By using multiple

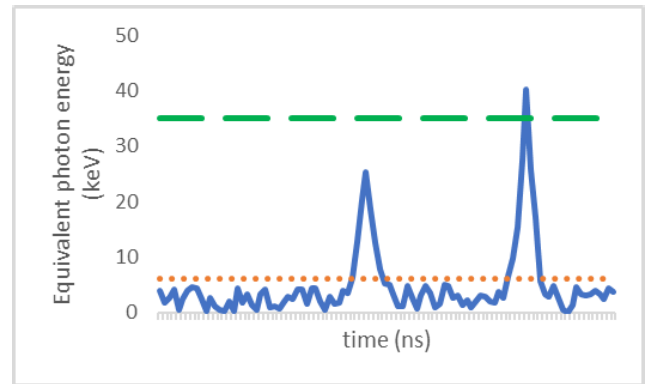


**FIGURE 1.** Example current (blue) from a pixel during a time window in which two photons are absorbed. Electronic noise is continuously present and random in nature, however relatively low in intensity. Energy integrating detectors calculate signal based on the area under the blue line, including the random noise. In contrast, PC detectors apply a threshold just above the noise floor (orange dotted line) so that counts from the noise can be entirely suppressed. Application of subsequent thresholds (green dashed line) allow for the discrimination of incoming photons based on energy.

energy thresholds, an x-ray photon counting spectral imaging (x-CSI) approach can be used, whereby the spectral overlap between low and high energy bins is greatly reduced, and far more energy bins can be reconstructed (up to 8 in some implementations [5]) compared with the 2 in dual energy set-ups. This allows for a range of benefits, including better material decomposition [6], soft tissue contrast, and lower flux rates to be achieved for a given image quality [7].

x-CSI detectors introduce new challenges compared with EI detectors however, which pose very different constraints when optimising pixel dimensions. These difficulties, and the constraints they apply are:

1). Temporal. In order to distinguish between individual incident photons, the time interval between successive incident photon interactions on a single pixel,  $t_i$ , should be greater than the time required to shape and read out a signal pulse from that pixel,  $t_s$ . Due to the stochastic nature of photon interactions with the sensor however, it is in practice necessary to make  $t_i$  much greater than  $t_s$ , to minimise the chance of two separate photons interacting in a single pixel at the same time:

$$t_i \gg t_s \quad (1)$$

At medically relevant x-ray fluxes, this requires very high counting rates from the electronics, with shaping times of the order of tens of nanoseconds [8]. To cope with this it is noted that, for a given x-ray flux, the value of  $t_i$  can be increased by reducing the pixel size both in terms of pixel pitch and pixel thickness. Reduction in pixel thickness reduces collection efficiency however, and reduction in pixel pitch and thickness both contribute to an increase in spectral distortions [9].

2). Spectral. PC detectors attempt to classify the energy of incident photons, however the accuracy with which they can do this depends on a variety of factors including electric field distortions between pixel pads, the mean free path of

fluorescence photons in the sensor material, average depth of interaction, and the ratio of drift and diffusion velocities. Increasing pixel pitch will tend to reduce the extent of spectral distortions due to a reduction in the probability of charge sharing events, though some will remain even for very large pixel pitches.

Most x-CSI application specific integrated circuits (ASICs) currently available or in development address the high-count rate requirements by utilising small pixels (compared with conventional EI detectors), however this further increases the spectral distortions present in such detector. To compensate for this, some groups implement a charge sharing correction algorithm (CSCA) in their ASICs. A wide variety of such algorithms have been proposed, however all essentially work by trying to identify where a single photon has deposited its energy across multiple pixels and adjusting the counters accordingly to try to reduce the spectral distortion created. CSCAs are not perfect and there are charge loss situations where they will intrinsically over or under compensate, however their benefit in reducing spectral distortions has been well established [10] and their limitations studied [11], [12].

The above discussion illustrates that in the case of x-CSI detectors there are competing demands on pixel size, such that deciding which of two pixel geometries is better for a given application is difficult to solve with a purely analytical approach. Further, whilst optimisation of pixel geometries for a variety of medical scanners using Monte Carlo simulations has been reported before for a variety of detectors [13]–[15], the case of x-CSI detectors is more complicated as the presence or absence of a CSCA can make a large difference to the detector performance.

Attempts have been made to model the spectral response of x-CSI detectors utilising analytical [16], Monte Carlo [17] or a combination of both techniques [18], [19]. These approaches usually assess some subset of the variables, most commonly pixel pitch, whilst keeping other variables such as thickness and flux constant. The varying approaches are often difficult to compare directly due to differences in the parameters varied, assumptions built in (notably whether pileup is included) and the metrics against which they are assessed. These differences partly stem from whether the studies are focusing on improving ASIC designs [20] or demonstrating the potential benefits of x-CSI to a particular clinical task [21]. In order to facilitate more consistent comparisons between the major detector parameters and their effects on detector performance this a single framework which allows all of these parameters to be varied and compared to a set list of metrics is needed. The project that the work in this paper derives from involves the systematic variation of pixel pitch, pixel thickness and CSCA type to compare 715 different systems at 4 different flux levels. In total this project investigates 2860 different simulations which have been designed based on the same assumptions so as to maximise comparability. Due to the complexity of this project it is divided into several publications, each assessing a subset of the variables and attempting to extract general trends from them.

In the present publication we consider the effect of pixel pitch and thickness, for the case of a single flux without CSCA, to establish general trends in x-CSI detector performance based on a range of x-CSI relevant metrics. A subset of results considering application of a single CSCA and two additional fluxes are included within this paper for the purpose of elucidating the mechanisms behind identified trends. Detailed comparisons of CSCAs and the behaviour of observed trends at varying fluxes will be considered in subsequent publications.

## II. METHODS

### A. SIMULATION FRAMEWORK

This work utilises an in-house simulation package referred to as CoGI (**C**omsol-**G**ate **I**nterlocutor). The details of CoGI and its experimental validations have been reported on previously [22], [23]. In summary, CoGI uses Monte Carlo (built on GATE [24]), finite element (built on COMSOL [25]) modelling techniques, and custom Matlab scripts (referred to as SGS) to simulate the imaging chain of a planar x-CSI detector, from x-ray emission and interaction with matter, through charge cloud drift and signal induction, to CSCA application and image/energy spectrum output, as illustrated in Fig. 2. Previous work has demonstrated that CoGI was able to model the proprietary CSCA employed by XCounter's Actaeon series PC detector [23], [26], and in its current form CoGI can now model 13 different CSCAs.

### B. MONTE CARLO SIMULATION PARAMETERS

All Monte Carlo simulations were performed with the same random seed to produce the exact same incident photon properties and initial interactions for all geometries, so that the variation between the different simulations would be based on geometric factors rather than differences from the random number generator.

**Geometry:** The Monte Carlo simulations involved the definition of a rectangular wafer of CdTe to represent the sensor. All simulations were performed modelling a wafer with 21 mm × 21 mm cross sectional area, however the thickness of the wafer was varied between 1 and 3 mm, in 0.5 mm increments, across different simulations. This range of thicknesses was selected as it covers the CdTe/CZT thicknesses currently being investigated for photon counting detectors in the field of medical CT system design [9], with an additional step either side to allow for future developments towards either thinner or thicker pixels.

These wafers were then exposed to a flat field irradiation from a rectangular source slightly larger than the cross section of the CdTe wafer (24 mm × 24 mm).

**Irradiation:** The photons from the source were perpendicularly incident on one of the larger area faces of the wafer and monoenergetic in nature (80 keV). This energy was chosen because it is close to the k-edge of gold (which is of interest to other work going on within our group) and is sufficiently high energy to allow good separation between photopeak,

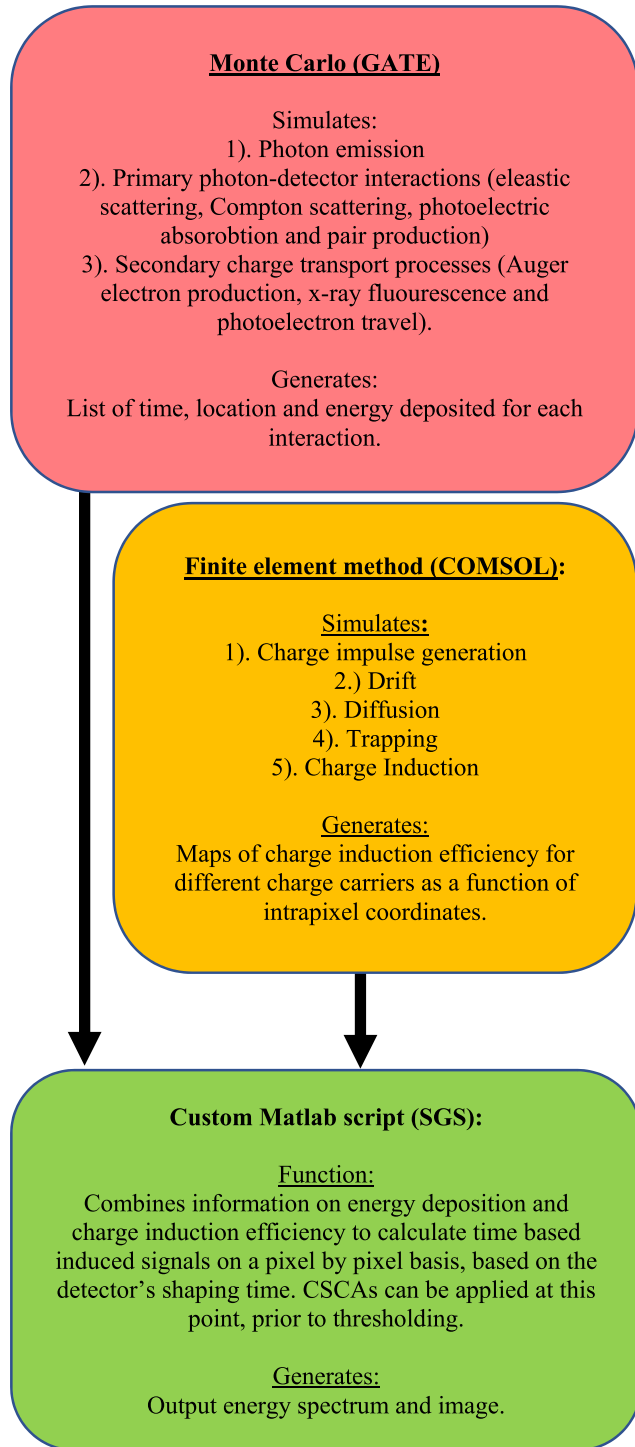


**FIGURE 2.** Schematic representation of the workflow performed by CoGI. Monte Carlo simulations are performed using the open source GATE software to model photon generation and interaction with matter. In parallel, the commercial finite element method program COMSOL is used to determine charge collection efficiencies as a function of time and location within the crystal. The output of the above two works are then exported into a custom Matlab code which handles signal integration and CSCA application, as well as allowing pile-up effects to be incorporated.

escape, and fluorescence peaks whilst still remaining in the medically relevant range of x-ray energies (<140 keV). Irradiations with different temporal profiles were defined such

that each geometry was irradiated at 4 different fluxes:  $\sim 10^6$ ,  $10^7$ ,  $10^8$ , and  $10^9$  photons  $s^{-1} mm^{-2}$ . The duration of the irradiation was set so that the total number of photons incident on the sensor would be constant between the different fluxes and provide sufficient photons to keep uncertainty due to the Poisson statistics of the Monte Carlo simulation < 0.1% (minimum number of photons absorbed in photoelectric interactions in any given sensor simulation was  $\sim 1.7$  million events).

**C. FINITE ELEMENT METHOD SIMULATION PARAMETERS**

The finite element model was used to simulate the charge induction efficiency (CIE) of the various pixel pitch-thickness combinations, by implementing Prettyman's adjoint continuity equations [27], as described in our previous works [28], [13], [22]. CIE is defined as

$$CIE = q/Q \tag{2}$$

where Q is the free charge produced in the detector by the ionising interaction of an incident photon and q is the charge induced at the collecting electrode due to the movement of these free charges. As per the most recent incarnation of CoGI, the CIE values from both electrons and holes were calculated separately and then combined into a final map of CIE as a function of pixel location. We selected a prototype detector we have experience within our lab (belonging to the XCounter Actaeon series of detectors, utilizing CdTe as a sensor material) to determine the bias voltage, pixel pad spacing, and shaping time parameters to use for one of the pixel geometries. The details of this system are proprietary information and so will not be discussed further here. We refer to this pixel geometry as geometry- $\alpha$ . The parameters for the other pixel geometries were then determined based on geometry- $\alpha$  so that the drift time and pixel pad spacing would be held constant. In practice this meant that the bias voltage for a pixel geometry x was calculated according to the equation:

$$V_x = V_\alpha (T_x/T_\alpha)^2 \tag{3}$$

where T refers to the pixel thickness, V refers to the bias voltage and the subscripts x and  $\alpha$  refer to the geometry being calculated and the reference geometry respectively.

**D. SGS PARAMETERS**

The Monte Carlo results for a given sensor thickness and x-ray flux were imported into SGS, which then handled the process of pixelating the output and converting all recorded events into normalised intrapixel coordinates, for comparison with the relevant CIE maps. This process reduced the number of Monte Carlo simulations that needed to be run and more realistically reflects the physics of a CdTe sensor as it did not force the Monte Carlo simulation to assess absorption at pixel boundaries, which provides a potential source of error in other simulations if not implemented correctly. The pixelated data was then combined with the relevant CIE maps to generate a

list of induced charges across the pixel array at a given time. CSCA can be applied to the data set at this point, to replicate pre-thresholding charge summing. Finally, the output signals for each pixel are compared with pre-set thresholds and relevant counters incremented. It should be noted that in physical detectors a signal would increment the counts on all counters whose threshold it passes, and the counts in each bin need to be calculated by subtraction. For computational efficiency this two-step binning approach was replaced with a direct binning scheme in which a signal was assigned to the relevant energy bin directly. Either implementation is available in CoGI however the large amount of data processed in this experiment warranted the more time efficient method be used. For the same reason, in contrast to the case with our previously published work, the differences in electric field for edge and corner pixels were neglected.

### E. SELECTION OF ENERGY BIN THRESHOLDS

The energy spectra for all combinations of thickness, pitch, flux, and CSCA were assessed preliminarily, both to ensure that the major spectral features (photopeak, escape peak, fluorescence peak, coincidence peaks etc.) were present, and also to ascertain whether energy calibration would be required for the various detector setups (as would be the case if the spectral features varied from their expected locations significantly). The photopeak locations were determined based on Gaussian functions fitted to the photopeaks. During this preliminary work it was discovered that whilst this approach works well for most pixel geometries, extreme pixel geometries yielded photopeaks that were poor fits to a single Gaussian model. This was due to three main factors:

- 1). Due to the relatively low x-ray photon energies associated with medical x-ray applications, there is little separation between the photopeak and the Compton continuum.
- 2). At extremely large values for the ratio of pixel pitch to thickness, CIE values deviated from unity in a significant part of the pixel volume, resulting in significant low energy tailing effects from CIE alone.
- 3). At extremely small values of pixel pitch and thickness, the probability of full photopeak capture within a single pixel is sufficiently low that the photopeak was comparable in size or even smaller than the low energy tail.

Collectively, these factors result in the gaussian approximation for the main photopeak being insufficient for many of the simulated systems, with the more detailed Voigt functions being required to ensure a good fit in these systems. Due to the added uncertainty associated with fitting these functions in situations where the photopeak height is small compared with the low energy tail, it was decided not to use spectral metrics such as energy resolution at all for the current work. Instead, in order to better reflect the operational realities of x-CSI detectors, it was decided that the detectors would be simulated operating in a binned collection mode. This had the added benefit of ensuring the metrics being compared were clearly and consistently defined between all geometries. Four energy bins were simulated, the smallest number required to

isolate the identified spectral features whilst still being realistic based on current technological capabilities/ambitions in x-CSI. Exhaustive searching of the spectra generated by CoGI and comparison with the Monte Carlo results they are based on revealed that whilst counts due to the complete deposition of photons of energy  $E$  may register in the detector at a range of energies less than  $E$  (due to charge loss from diffusion effects or carrier trapping etc), they almost never register at energies above  $(E + 1.5)$  keV. For this reason, it was decided that the spectra would be binned as follows:

- i). 10 keV was selected as the noise floor, above which a signal needs to rise to be registered in the detector at all. Signals registering below this level were suppressed.
- ii). Signals corresponding to  $E$  of between 10 keV and 30 keV were placed into bin 1: the 'fluorescence bin'. This bin should contain all of the events due to Cd fluorescence x-ray capture ( $\sim 23$  keV and  $\sim 26$  keV photons).
- iii). Signals corresponding to  $E$  of between 30 keV and 60 keV were placed into bin 2: the 'escape bin'. This bin should contain almost all of the photons in the escape peaks of the spectra.
- iv). Signals corresponding to  $E$  of between 60 keV and 83 keV were placed into bin 3: the 'photopeak bin'. This bin should contain almost all of the photons in the main photopeak of the spectra.
- v). Signals corresponding to  $E$  greater than 83 keV were placed into bin 4: the 'coincidence bin'. Signals in this bin will exclusively be the result of multiple photons interacting with a single pixel and being summed together.

### F. METRICS USED FOR COMPARING SIMULATED DETECTORS

In this work we will consider four metrics proposed for assessing the performance of x-CSI detectors. The different sensor geometries will be compared based on their absolute detection efficiency, absolute photopeak bin efficiency, spectral efficiency, and fractional coincidence counts. In assessing these metrics, results from all pixels are pooled into a single data set, representing the average behaviour of the sensor as a whole. The metrics are defined as follows:

Absolute Detection Efficiency (ADE): The ratio of all counts in the detector to the number of incident photons.

$$\text{ADE} = \sum_{E=1}^4 B_E / I \quad (4)$$

where  $B_E$  is the number of counts in bin  $E$  and  $I$  is the number of photons that impinge upon the sensor (given by flux multiplied by area of sensor).

Absolute Photopeak bin Efficiency (APE): The ratio of counts in the photopeak bin to number of incident photons.

$$\text{APE} = B_3 / I \quad (5)$$

where  $B_3$  is the number of counts in the photopeak bin.

Relative Coincidence Counts (RCC): The ratio of events in the coincidence bin to counts in all bins. This is a measure of

the effects of pulse pile-up.

$$RCC = B_4 / \sum_{E=1}^4 B_E \tag{6}$$

where  $B_4$  is the number of counts in the coincidence bin.

Binned Spectral Efficiency (BSE): The ratio of counts in the photopeak bin to the counts across all bins.

$$BSE = B_3 / \sum_{E=1}^4 B_E \tag{7}$$

**G. DIVISION OF RESULTS FOR ANALYSIS**

The work this paper is based on represents an extensive study across four degrees of freedom (thickness, pitch, flux, CSCA) and as such there are considerable ways in which the results could be analysed. In order to prevent the dimensionality of the analysis becoming cumbersome, the data will be analysed in a series of papers. This paper represents part one of this analysis and will concern itself with the effect of pixel geometry (thickness and pitch) on the stated metrics at a single flux (~10<sup>7</sup> photons s<sup>-1</sup> mm<sup>-2</sup>), and without the application of CSCAs. This will allow for a more in-depth discussion of the possible mechanisms behind identified trends. Results from situations of differing flux or CSCA may be invoked to support the proposed mechanisms where necessary, however an extensive discussion of the role flux and CSCA choice play in shaping the above metrics will be tackled in subsequent publications.

**III. RESULTS**

As discussed previously, the results shown in this section concern a single flux (~10<sup>7</sup> photons s<sup>-1</sup> mm<sup>-2</sup>) and are raw data readouts from the sensors, with no charge sharing correction algorithms applied, unless otherwise stated in the figure captions.

Fig. 3 shows how ADE varies as a function of pitch for the 5 different thicknesses considered in this work. The main trends evident in this plot that need explanation are the trend towards decreasing ADE as pixel pitch increases and the trend towards increasing ADE as pixel thickness increases. It is of note that neither of these trends is linear in nature and that for many of the geometries shown the ADE is greater than 100%. This is due to how ADE is defined, as will be explained in the discussion section.

Figs. 4 and 5 illustrate how APE varies as functions of pixel pitch and thickness. Fig. 4 shows the relations for the raw data whilst Fig. 5 shows the effect on the trends of applying a 3 pixel × 3 pixel dynamic reconstructive (3 × 3 Dy) CSCA to the data pre-thresholding. 3 × 3 Dy refers to a CSCA that works as follows:

- 1). An event is detected in a pixel.
- 2). Events are searched for in adjacent pixels (including diagonals) that occur within a short time window (100 ns in this example) of this initial signal. This produces a 3 pixel by 3 pixel search area.
- 3). Events identified across the search area within the time window are then summed together as a single event.

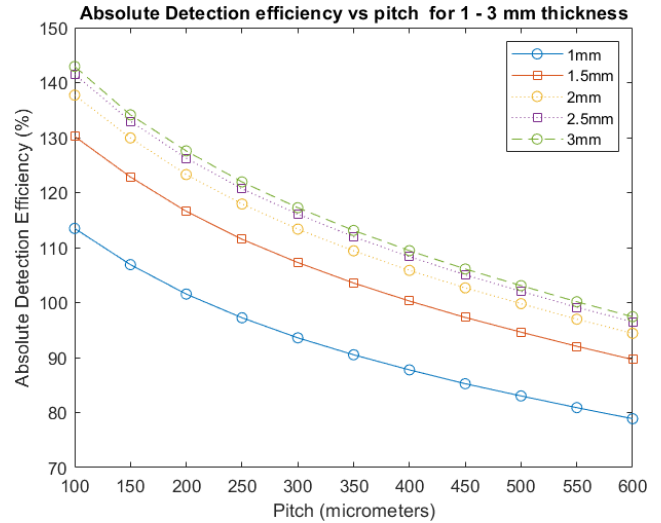


**FIGURE 3.** Plot of absolute detection efficiency as a function of pixel pitch and pixel thickness at a flux of 10<sup>7</sup> photons mm<sup>-2</sup> s<sup>-1</sup>. Detection efficiency is defined as counts recorded/photons incident.

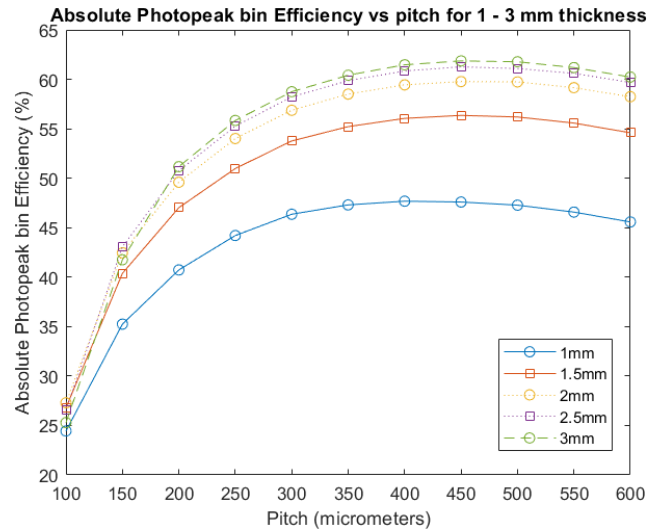
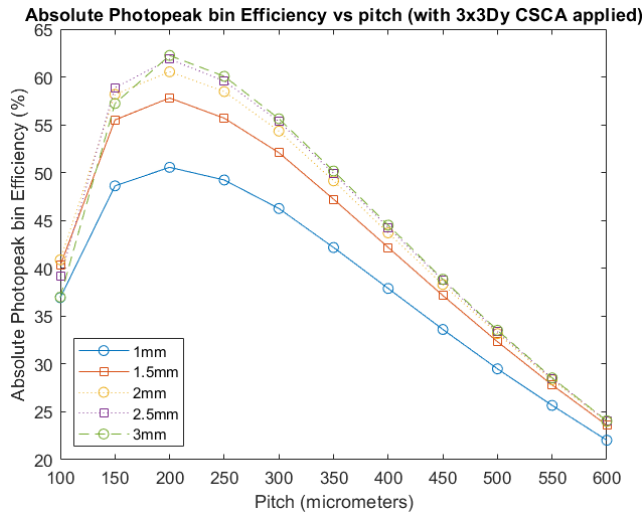


**FIGURE 4.** Plot of photopeak bin efficiency as a function of pitch and thickness at a flux of 10<sup>7</sup> photons mm<sup>-2</sup> s<sup>-1</sup>. Photopeak bin efficiency is defined as the counts recorded in the photopeak bin/photons of 80 keV incident on detector.

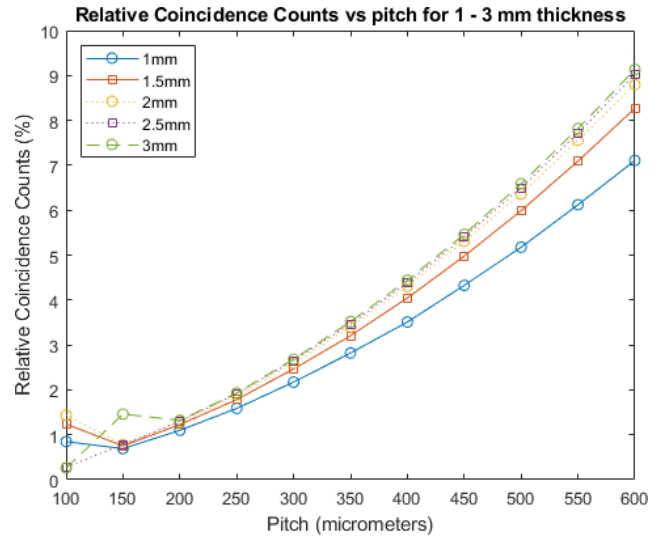
This is done based on the assumption that such events are likely to be the result of charge sharing mechanisms from a single initial event, due to their temporal and spatial proximities.

Fig. 5 is included at this stage simply to support assertions made in the discussion section as to the mechanism behind trends of interest in this data set. Detailed discussion on the effects of different CSCAs on this and other metrics can be found in subsequent publications. The main trends evident in Fig. 4 that need explanation are the increase in APE with increasing pixel thickness and the convex relation between pixel pitch and APE. Fig. 5 shows the same convex behaviour as Fig. 4, however with a much greater degree of curvature.

Figs. 6, 7 and 8 are plots of the percentage of counts recorded by the detector that get assigned to the coincidence



**FIGURE 5.** Plot of photopeak bin efficiency as a function of pitch and thickness at a flux of  $10^7$  photons  $\text{mm}^{-2} \text{s}^{-1}$ . Photopeak bin efficiency is defined as the counts recorded in the photopeak bin/photons of 80 keV incident on detector. In this case, a  $3 \times 3$  dynamic reconstructive CSCA has been applied.



**FIGURE 7.** Plot of relative coincidence counts as a function of pixel pitch and pixel thickness at a flux of  $10^7$  photons  $\text{mm}^{-2} \text{s}^{-1}$ . Relative coincidence counts are defined as the counts recorded in the coincidence bin/the sum of counts in all bins.

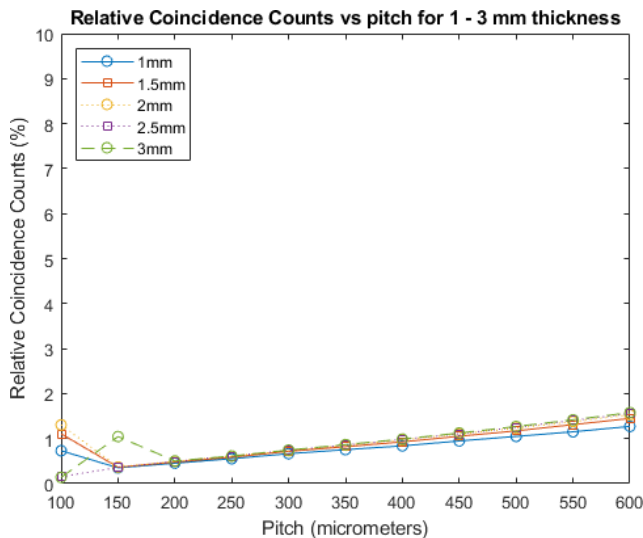


**FIGURE 6.** Plot of relative coincidence counts as a function of pixel pitch and pixel thickness at a flux of  $10^6$  photons  $\text{mm}^{-2} \text{s}^{-1}$ . Relative coincidence counts are defined as the counts recorded in the coincidence bin/the sum of counts in all bins.

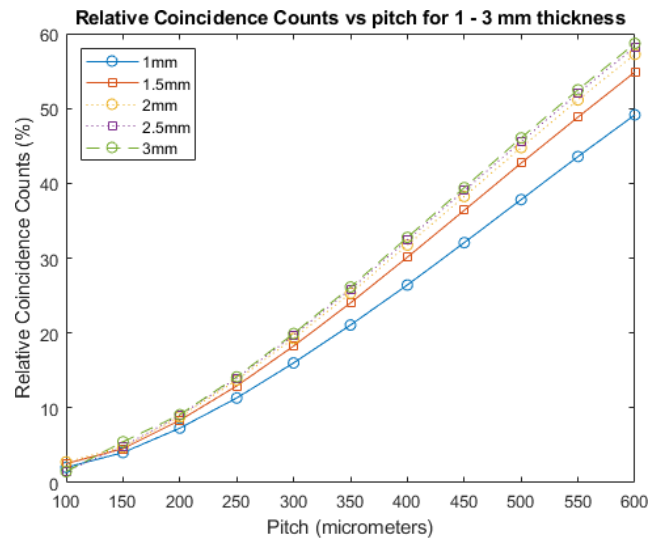


**FIGURE 8.** Plot of relative coincidence counts as a function of pixel pitch and pixel thickness at a flux of  $10^8$  photons  $\text{mm}^{-2} \text{s}^{-1}$ . Relative coincidence counts are defined as the counts recorded in the coincidence bin/the sum of counts in all bins.

bin (RCC), again as a function of pixel pitch and pixel thickness. Fig. 6 and Fig. 8 represent fluxes of  $10^6$  photons  $\text{mm}^{-2} \text{s}^{-1}$  and  $10^8$  photons  $\text{mm}^{-2} \text{s}^{-1}$  respectively. Fig. 7 represents a flux of  $10^7$  photons  $\text{mm}^{-2} \text{s}^{-1}$ , the same as the rest of the figures in this section. There are general trends evident of increasing coincidences recorded as pixel pitch or thickness increase. These trends are less evident at very low pixel pitches, and in particular the point at 3 mm thickness and 150  $\mu\text{m}$  pitch seems anomalous. These deviations will be discussed and Figs. 6 and 8 are included to facilitate this discussion.

Figs. 9 and 10 contain plots of BSE as a function of pixel thickness and pixel pitch, with Fig. 10 displaying the case

where a  $3 \times 3$  Dy CSCA is applied to the data. Trends in this figure are much less clear and are discussed in detail in the discussion section.

#### IV. DISCUSSION

In all of the discussions that follow it should be remembered that the exact values calculated will depend on a variety of factors such as operational bias voltages, material properties, shaping times, pixel pad spacing etc. that were fixed for these simulations but that represent additional degrees of freedom for anyone designing an x-CSI detector. The aim of this discussion is thus not to claim any absolute quantification of metrics such as “the spectral efficiency of all 200  $\mu\text{m}$  pitch and 3 mm thick pixels is  $x\%$ ,” but rather to identify trends

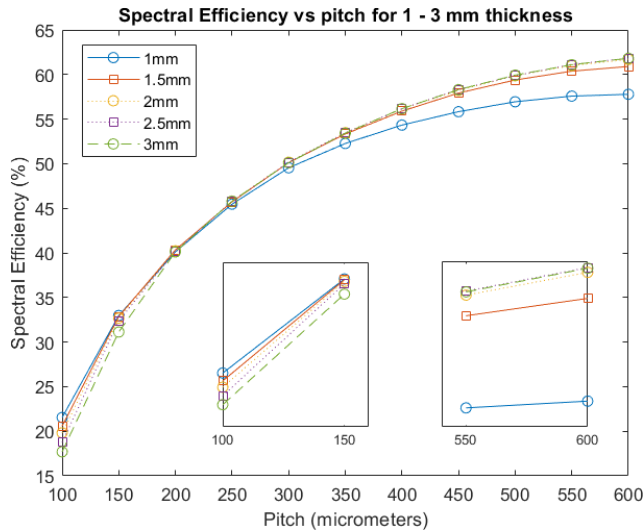


**FIGURE 9.** Plot of spectral efficiency as a function of pixel pitch and thickness at a flux of  $10^7$  photons  $\text{mm}^{-2} \text{s}^{-1}$ . The relation between efficiency and thickness is reversed between small (left inset) and large (right inset) pixel pitches.

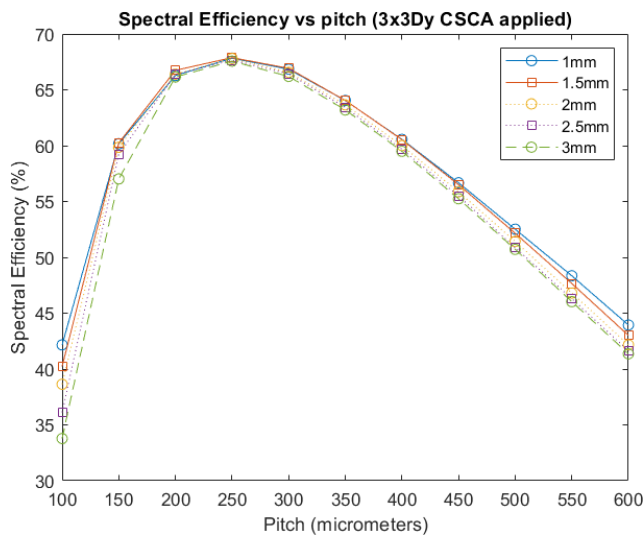


**FIGURE 10.** Plot of spectral efficiency as a function of pixel pitch and thickness at a flux of  $10^7$  photons  $\text{mm}^{-2} \text{s}^{-1}$ . Spectral efficiency is defined as the counts recorded in the photopeak bin/the sum of counts in all bins. In this case, a  $3 \times 3$  dynamic reconstructive CSCA has been applied.

present within the detector responses and to propose explanations as to the physical mechanisms likely responsible.

Initial ambitions for this work involved the fitting of Gaussian functions to the various photopeaks from the different detector parameters and using these peaks to compare spectral metrics of the various setups. The fitting of a Gaussian function to the photopeak is an approximation that is often used for determining energy resolution and other spectral metrics. As discussed in the methods section however, whilst this is a reasonable approximation for most of the geometries considered in this work, it is not a good fit to the most extreme thickness/pitch ratios e.g. 3 mm thickness, 100  $\mu\text{m}$  pitch. This is because in these situations, spectral

efficiency (the counts within the full-energy photopeak as a fraction of all counts in the detector, when running in spectral mode) is so low that the photopeak is almost completely obscured by counts from the Compton continuum and other events.

Fig. 3 shows how the ADE of the various sensors vary as a function of pixel pitch and thickness. The first thing to notice is that the ADE is greater than 100% for a large number of sensor geometries. The reason for this lies in the pixelated nature of the sensors, which allows for the possibility that a single photon could deposit its energy across multiple pixels (e.g. via x-ray fluorescence). This means that a single photon could give rise to more than one count and so the maximum ADE is greater than 100%. That clarified, we can proceed to discuss the trend in ADE seen with increasing pixel thickness and pitch.

The first trend to investigate is the ADE increase with increasing pixel thickness, for a given pixel pitch. Additionally, the increase appears to diminish exponentially with increasing thickness (the increase in ADE from 1 mm – 1.5 mm is much larger than that from 1.5 mm – 2 mm etc.). The reason for this behaviour is that as pixel thickness increases, so too does the path length for photons to cross through the sensor. As x-ray photon transmission through a material decreases exponentially with path length, this results in an increased number of events detected with increasing length, and also explains why the improvement in ADE of adding 0.5 mm thickness decreases as initial thickness increases.

The second trend in Fig. 3 that needs exploring is the decrease in ADE with increasing pixel pitch. This is due to a combination of two factors: reduction in Cd fluorescence x-ray escape and increasing probability of coincidence counts. Cd fluorescence x-rays can carry energy away from the initial site of interaction at any pixel pitch or thickness, however unless the fluorescence x-ray is absorbed in a different pixel to the site of the initial interaction it will not increase the number of counts in the detector as a whole and so will not contribute to an increase in ADE. Increasing pixel pitch reduces the probability that a fluorescence photon can escape the pixel of initial interaction and so reduces the chance that a single photon can register as more than one count in the detector. The effect of increasing pitch on ADE decreases exponentially with increasing pitch, again due to the fact that x-ray transmission drops off exponentially with path length, explaining the concaved shape of the decrease in ADE with pitch.

The second effect that contributes to the reduction in ADE with increasing pixel pitch is the increased probability of pulse pileup (coincidence events) with larger pixels at a given flux. The long-term behaviour of ADE as pixel pitch increases will depend on whether the detector is paralyzable (P) or non-paralyzable (NP) in nature. Both models will lead to ADE values approaching zero as ADE is expressed as % of actual flux, however P models will tend to zero much more quickly than NP models as their count rates drop off at high

per pixel fluxes rather than tending to a constant, non-zero value as P detectors do.

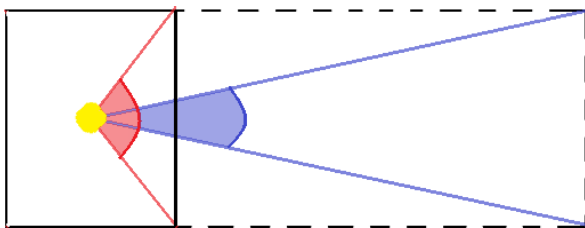
Fig. 4 illustrates how APE varies as functions of pixel pitch and thickness. Again there is a trend of increasing APE with increasing pixel thickness (with decreasing benefit to continuously increasing thickness), and again this is down largely to the increased path length afforded by the thicker pixels, as this is an absolute metric. The relation between APE and pixel thickness can be seen to be convex: with a positive gradient at lower pixel pitches but a negative gradient at larger pitches. We propose that the reason for this is that there are two competing effects at play and it is the balance between them that determines the gradient: charge sharing effects and pulse pile-up. Charge sharing effects accounted for in the simulation include x-ray fluorescence and partial charge cloud loss to diffusion out of the pixel of initial interaction. At small pixel pitches, the effect of lateral charge sharing between pixels, causes a significant reduction in the number of photons whose energy is deposited entirely in a single pixel. As pixel pitch increases however, the probability of charge sharing from x-ray fluorescence escaping the initial pixel of interaction or charge cloud diffusion decreases, resulting in an increase in APE. In contrast, pulse pile-up is negligible at low pixel pitches, but increases proportionally with pitch as it is proportional to the flux per pixel, so varies with pixel area under a constant flux. This leads to a reduction in APE as pitch increases. Together these factors result in the convex shape of the curve seen in Fig. 4. To support our claim that the interplay between charge sharing and pulse pile-up is responsible for the shape of this curve we include in this paper Fig. 5, which shows how the APE varies with pitch and thickness when a CSCA is applied (in this case a  $3 \times 3$  dynamic reconstructive algorithm). The curvature of the APE vs pitch line in Fig. 5 is significantly increased, leading to a peak at a much lower pitch. This is because CSCAs aim to reduce charge sharing effects but cannot determine if closely timed events in adjacent pixels are due to charge sharing across the pixels or coincidental, meaning that some of the reconstructed signals will be the sum of two unrelated photons. Consequently, CSCAs simultaneously reduce the effects of charge sharing and increase the effects of pulse pile-up. The increase in curvature of the fit upon application of a CSCA thus supports our assertion that the curvature is the product of competition between charge sharing and pulse pile-up effects. Further, it can be seen from Fig. 5 that thicker pixels have a steeper negative gradient at larger pixel sizes. This is consistent with the idea that it is pulse pile-up that is responsible for the decreasing APE at large pixel pitches as thicker pixels will absorb more photons at a given flux and so will suffer more severely in absolute terms from pile-up effects as pixel pitch increases.

Fig. 7 plots the number of counts in the coincidence bin as a function of both pixel thickness and pitch. As should be unsurprising given the discussion so far, coincidence counts increase as pitch increases (due to the consequent increase in flux per pixel) and also increase with increasing thickness

(due to the increase in path length, resulting in more photons being captured and a consequent higher probability that two or more photons arrive in the same pixel at the same time). What appears more surprising however is the behaviour of the points at the very low pitch values, with the 1 mm, 1.5 mm and 2 mm thicknesses yielding RCC values above what would be expected based on the trend from the larger pitches. It is initially tempting to suggest that the poor fit at these values is due to the increased uncertainty produced by the low number of photons arriving in coincidence ( $< 2\%$  of events), especially as the behaviour of detectors above  $200 \mu\text{m}$  is consistent with expectations based on our interpretation of the other metrics thus far. This would appear to be supported by the fact that these deviations are more pronounced at lower fluxes (Fig. 6) and less pronounced at higher fluxes (Fig. 8). The more difficult to explain deviation from expectation is seen in the RCC value of the 3 mm pixels at  $150 \mu\text{m}$  pitch, which spikes significantly higher than would be expected. This spike does not appear to be present at fluxes above  $10^8$  photons  $\text{mm}^{-2} \text{s}^{-1}$  (Fig. 8) and is less prominent in Fig. 7 than in Fig. 6 (1.9 times and 2.9 times higher than the 2.5 mm case respectively). This deviation may be a statistical artefact just as was the case with the  $100 \mu\text{m}$  points, or it may be related to some as-yet unelucidated mechanism operating at low fluxes. Further simulations involving significantly more incident photons and a changed random seed could be used to determine whether this event is statistical or not by increasing the counts in this bin without modifying the flux. Should this be ruled out, a further study looking at the step-by-step buildup of RCC counts in this and other pixel thicknesses at this pixel pitch may be needed to identify the precise cause of this unexpected result. These works would fall beyond the limits of the current study however and would take considerable time. Given the consistency of the explanations proposed so far for dealing with the trends observed, this point is therefore being provisionally treated as anomalous for the purposes of the current investigation.

Fig. 9 is arguably the most surprising figure generated by this work, however it is not immediately obvious that this is so. Superficially, Fig. 9 shows that changes in BSE as a function of pixel pitch are similar to the relation between APE and pixel pitch displayed in Figs. 4 and 5. In particular we note the same curved behaviour which we proposed is explained by the competition between charge sharing effects which dominate at low pixel pitches and pulse pile-up effects which dominate at larger pixel pitches. Fig. 10, which shows the effect of a  $3 \times 3$  dynamic reconstructive CSCA on BSE, can be used to support this interpretation in a similar way to how Fig. 5 supports Fig. 4 (see above). There are however some very important distinctions between the trends evident in Figs. 9 and 4. Evidently the effect of pixel thickness is not as clear cut as was the case with APE. Initially it appears that thickness has little effect on BSE for most pixel pitches, and this seems immediately sensible given the differing denominators in the definitions of the two metrics. In the case of APE the divisor is the number of incident

photons, so it stands to reason that as the sensor thickness increases, a higher proportion of all photons is captured and so a higher APE results. In BSE however the denominator is the counts in all energy bins, so simply doubling the number of photons absorbed would not affect the fraction of those photons that end up in the photopeak bin, all else being equal. All else cannot be equal however, as careful examination of the low and high pixel pitch values (Fig. 9 insets) reveals that there is indeed a dependence of BSE on thickness, but it is not a straightforward one. It can be seen in Fig. 9 that the relation between pixel thickness and BSE inverts: at small pixel pitches BSE increases for thicker pixels, whilst at larger pixel pitches BSE decreases for thicker pixels. This behaviour is not seen in any of the other metrics assessed, and the more complicated relation requires explanation. We propose that the reason for this lies specifically with the subset of charge sharing effects mediated by Cd fluorescence x-rays. Consider the situation in which a fluorescence photon is emitted from a charge cloud, as shown in Fig. 11. Such a fluorescence photon has three possible fates:



**FIGURE 11.** When a fluorescence photon is produced (yellow circle) the direction of its emission is random. In thinner pixels (solid lined box) there are more possible angles of escape from the sensor (red angle) than there are in thicker pixels (purple angle and dashed line).

- 1). The fluorescence photon could be reabsorbed within the same pixel, in which case the photopeak bin counter will be incremented, and the BSE will increase.
- 2). The fluorescence photon could escape from the sensor entirely without being reabsorbed, in which case the escape bin will be incremented, and the BSE will drop.
- 3). The fluorescence x-ray could escape the primary pixel of interaction but be captured in an adjacent pixel. In this case the escape bin and fluorescence bins would both be incremented, decreasing BSE.

It should be noted that whilst outcomes 2 and 3 above both reduce BSE, outcome 3 reduces it to a greater extent. The reason for this is that BSE is defined as the number of counts in the photopeak bin divided by the sum of counts in all bins, and outcome 3 produces two counts outside of the photopeak bin whilst outcome 2 only produces one. The argument can then be made as follows. At low pixel pitches we can expect charge sharing effects to be more significant, so we consider the relative likelihood of outcomes 2 and 3. In order for outcome 2 to occur the fluorescence x-ray must escape from the end of the sensor. For a small pixel thickness (solid lined box in Fig. 11) the solid angle within which a fluorescence photon would escape the sensor before crossing into another

pixel is relatively large, as indicated by the red angle. When the pixel is thicker however (dashed box in Fig. 11) the range of angles over which a fluorescence photon could be emitted such that it escapes the sensor before crossing into another pixel is smaller.

Assuming isotropic emission of the fluorescence x-ray, this implies that the probability of a fluorescence x-ray experiencing outcome 3 increases with increasing pixel thickness. Consequently we would predict that thicker pixels would tend to have lower BSE at low pixel pitches, as seen. Note that this effect is not observed for APE, as only the counts in the photopeak bin are used in calculating APE, so outcomes 2 and 3 are indistinguishable by this metric.

As pixel pitch increases, the number of fluorescence photons undergoing outcome 3 decreases as a lower proportion of the potential interaction locations within the pixel are close enough to the edge of the pixel that a fluorescence photon could cross before being reabsorbed. At these pitches fluorescence photons will not degrade BSE unless they are able to escape the sensor entirely. The geometric arguments made with the help of Fig. 11 should convince the reader that in this case, thicker pixels will tend to have higher SEs, as they reduce the proportion of angles in which fluorescence photons can travel to escape the pixel. The increasing thickness will also reduce the probability of a photon escaping the pixel even if it is emitted in the correct direction, as it will increase the path length of the photon through the sensor material.

Collectively, the above points constitute our argument for the inversion of the relation between pixel thickness and BSE observed in Fig. 9. In order for this explanation to be concordant with our previous arguments concerning the other metrics, it would be necessary that, at sufficiently large pixel pitches, pile-up effects begin to deteriorate the SE, and moreover that they should affect the thicker pixels more severely. Whilst we do not have data for pixels at greater pitches than  $600 \mu\text{m}$ , we have previously established that the application of a CSCA can have a similar effect as a greater pixel pitch in that it increases the severity of pile-up effects. Fig. 10 shows how BSE varies in the simulation when a  $3 \times 3$  Dy CSCA is employed. This figure shows that, as expected, as pulse pile-up effects begin to dominate (larger pixel sizes) the thicker pixels exhibit lower BSE than the thinner ones.

This work has considered the performance of the simulated systems with respect to 4 energy-based metrics as x-CSI is fundamentally an energy sensitive technique, but also because other works in this area assess detectors according to similar metrics. It should be noted however that the intended application needs to be kept in mind when deciding on the optimal configuration for a system. Larger pixel pitches may reduce charge sharing effects, improving energy resolution but will also reduce the spatial resolution of the images produced. Similarly, thicker pixels may produce higher photopeak efficiencies, but they do so at a cost of spatial resolution. This is because thicker pixels are associated with more significant lateral diffusion and the detection of a higher number of oblique angled x-rays. Additionally, even where

thicker pixels are desirable, the physical realities of production mean that thicker crystals are usually less uniform, with an increased risk of crystal defects that can cause local trapping, degrading individual pixel performance and overall image quality.

Similarly, the work presented here has considered the case of a monoenergetic field in a way that is consistent with approaches to physical x-CSI detector assessment undertaken by other groups [11], [20], as it is easier to assess spectral performance in physical systems using monoenergetic or discretised sources such as a synchrotron or radioisotopes. Clinical applications usually involve the use of a polychromatic beam, however spectral metrics will have an impact on final system performance, when it comes to energy dependent tasks such as material decomposition. Further, as initial charge cloud size will vary as a function of energy, the exact impact of charge sharing on system output will vary as the energy used is altered. This adds significant complication for the case of a polychromatic incident beam, and such effects will need to be accounted for in future work.

Consequently, whilst this work investigates the optimisation of x-CSI detectors for spectral performance, full system design will need to additionally be informed by task specific requirements, and a tradeoff between spatial resolution and energy resolution will likely be needed. Nevertheless, the work presented here shows the value of CoGI as a simulation framework for evaluating such tradeoffs, and in principle any desired task specific metric could be addressed in a similar way, including those that rely on a polychromatic irradiation.

## V. CONCLUSION

This publication has focussed on the effect of pixel pitch and thickness on a range of x-CSI specific metrics: specifically, absolute detection efficiency, absolute photopeak bin efficiency, spectral efficiency, and relative coincidence counts. The simulations performed demonstrate the versatility of CoGI, with this work constituting firstly a proof of principle that a wide range of different x-CSI detector geometries can be modelled using a single simulation framework. Whilst a monoenergetic irradiation was considered here both for ease of analysis and to be consistent with other work in this area, CoGI is equally capable of simulating polychromatic irradiations. This is currently reserved for assessing task specific metrics where the polychromatic beams would be used clinically.

Trends in the relation between each metric and each geometric parameter (pitch and thickness) were identified and explanations proposed based on physical mechanisms. Where the trends were unexpected or counter intuitive, CSCAs were used to investigate the potential mechanisms and support the development of a proposed explanation. In particular, the widely different results obtained when considering absolute photopeak efficiency and spectral efficiency underline the importance of selecting the most appropriate metric for testing prototype detectors, as the best metric will likely be

application specific. Further, the identification of a break down at extreme thickness/pitch ratios of the assumption that photopeaks can be fitted with a Gaussian illustrates the importance of caution in applying assumptions from other spectroscopic techniques to x-CSI.

The work covered in this publication is a subset of a larger study in which not only thickness and pitch but also x-ray flux and applied CSCA are varied, and trends in their effect on relevant metrics assessed. Due to the many degrees of freedom available in analysing this larger data set however, the work was split into several publications, and whilst this one considers only pixel pitch and thickness, subsequent publications based on this data set will investigate the effect of flux (from  $10^6 - 10^9$  photons  $s^{-1} mm^{-2}$ ) and CSCA choice on the above metrics as well as some new ones more suitable to these new variables.

## REFERENCES

- [1] A. N. Primak, J. C. Ramirez Giraldo, X. Liu, L. Yu, and C. H. McCollough, "Improved dual-energy material discrimination for dual-source CT by means of additional spectral filtration," *Med. Phys.*, vol. 36, no. 4, pp. 1359–1369, Mar. 2009.
- [2] I. Mori, Y. Machida, M. Osanai, and K. Inuma, "Photon starvation artifacts of X-ray CT: Their true cause and a solution," *Radiol. Phys. Technol.*, vol. 6, no. 1, pp. 130–141, 2013.
- [3] K. Taguchi and J. S. Iwanczyk, "Vision 20/20: Single photon counting X-ray detectors in medical imaging," *Med. Phys.*, vol. 40, no. 10, Sep. 2013, Art. no. 100901.
- [4] T. Koenig, J. Schulze, M. Zuber, K. Rink, J. Butzer, E. Hamann, A. Cecilia, A. Zwerger, A. Fauler, M. Fiederle, and U. Oelfke, "Imaging properties of small-pixel spectroscopic X-ray detectors based on cadmium telluride sensors," *Phys. Med. Biol.*, vol. 57, no. 21, p. 6743, 2012.
- [5] R. Ballabriga, J. Alozy, G. Blaj, M. Campbell, M. Fiederle, E. Frojdh, E. H. M. Heijne, X. Llopart, M. Pichotka, S. Procz, L. Tlustos, and W. Wong, "The Medipix3RX: A high resolution, zero dead-time pixel detector readout chip allowing spectroscopic imaging," *J. Instrum.*, vol. 8, no. 2, Feb. 2013, Art. no. C02016.
- [6] L. K. Stamp, N. G. Anderson, F. Becce, M. Rajeswari, M. Polson, O. Guyen, A. Viry, C. Choi, T. E. Kirkbride, and A. Y. Raja, "Clinical utility of multi-energy spectral photon-counting computed tomography in crystal arthritis," *Arthritis Rheumatol.*, vol. 71, no. 7, pp. 1158–1162, 2019.
- [7] S. Si-Mohamed, D. Bar-Ness, M. Sigovan, D. P. Cormode, P. Coulon, E. Coche, A. Vlassenbroek, G. Normand, L. Boussel, and P. Douek, "Review of an initial experience with an experimental spectral photon-counting computed tomography system," *Nucl. Instrum. Methods Phys. Res. A, Accel. Spectrom. Detect. Assoc. Equip.*, vol. 873, pp. 27–35, Nov. 2017.
- [8] *Confidential Personal Communications With Various X-CSI ASIC Designers (2018–2019)*.
- [9] R. Ballabriga, J. Alozy, F. N. Bandi, M. Campbell, N. Egidios, J. M. Fernandez-Tenllado, E. H. M. Heijne, I. Kremastiotis, X. Llopart, B. J. Madsen, D. Pennicard, V. Sriskaran, and L. Tlustos, "Photon counting detectors for X-ray imaging with emphasis on CT," *IEEE Trans. Radiat. Plasma Med. Sci.*, early access, Jun. 16, 2020, doi: 10.1109/TRPMS.2020.3002949.
- [10] T. Koenig, M. Zuber, E. Hamann, A. Cecilia, R. Ballabriga, M. Campbell, M. Ruat, L. Tlustos, A. Fauler, M. Fiederle, and T. Baumbach, "How spectroscopic X-ray imaging benefits from inter-pixel communication," *Phys. Med. Biol.*, vol. 59, no. 20, pp. 6195–6213, Oct. 2014.
- [11] C. Ullberg, M. Urech, C. Eriksson, A. Stewart, and N. Weber, "Photon counting dual energy X-ray imaging at CT count rates: Measurements and implications of in-pixel charge sharing correction," *Proc. SPIE*, vol. 10573, Mar. 2018, Art. no. 1057319.
- [12] M. C. Veale, S. J. Bell, D. D. Duarte, A. Schneider, P. Seller, M. D. Wilson, and K. Iniewski, "Measurements of charge sharing in small pixel CdTe detectors," *Nucl. Instrum. Methods Phys. Res. A, Accel. Spectrom. Detect. Assoc. Equip.*, vol. 767, pp. 218–226, Dec. 2014.

- [13] P. Guerra, A. Santos, and D. G. Darambara, "Development of a simplified simulation model for performance characterization of a pixelated CdZnTe multimodality imaging system," *Phys. Med. Biol.*, vol. 53, no. 4, pp. 1099–1113, Feb. 2008.
- [14] M. E. Myronakis and D. G. Darambara, "Monte Carlo investigation of charge-transport effects on energy resolution and detection efficiency of pixelated CZT detectors for SPECT/PET applications," *Med. Phys.*, vol. 38, no. 1, pp. 455–467, Dec. 2010.
- [15] D. Maneuski, V. Gostilo, and A. Owens, "TCAD simulation studies of novel geometries for CZT ring-drift detectors," *J. Phys. D, Appl. Phys.*, vol. 53, no. 1, Jan. 2020, Art. no. 015114.
- [16] K. Taguchi, K. Stierstorfer, C. Polster, O. Lee, and S. Kappler, "Spatio-energetic cross-talk in photon counting detectors: Numerical detector model (Pc TK) and workflow for CT image quality assessment," *Med. Phys.*, vol. 45, no. 5, pp. 1985–1998, 2018.
- [17] S. S. Hsieh, P. L. Rajbhandary, and N. J. Pelc, "Spectral resolution and high-flux capability tradeoffs in CdTe detectors for clinical CT," *Med. Phys.*, vol. 45, no. 4, pp. 1433–1443, Apr. 2018.
- [18] M. Persson, A. Wang, and N. J. Pelc, "Detective quantum efficiency of photon-counting CdTe and Si detectors for computed tomography: A simulation study," *J. Med. Imag.*, vol. 7, no. 4, p. 1, Jul. 2020, doi: 10.1117/1.JMI.7.4.043501.
- [19] K. Stierstorfer, "Modeling the frequency-dependent detective quantum efficiency of photon-counting X-ray detectors," *Med. Phys.*, vol. 45, no. 1, pp. 156–166, Jan. 2018.
- [20] P. Trueb, P. Zambon, and C. Broennimann, "Assessment of the spectral performance of hybrid photon counting X-ray detectors," *Med. Phys.*, vol. 44, no. 9, pp. e207–e214, Sep. 2017.
- [21] Y. Pavia, A. Brambilla, V. Rebuffe, N. Freud, J. M. Létang, and L. Verger, "Breast density and iodine quantification in spectral mammography," *Biomed. Phys. Eng. Express*, vol. 4, no. 1, 2017, Art. no. 015008.
- [22] O. P. Scienti, A. Shah, J. Bamber, and D. Darambara, "An assessment of photoacoustic and photon counting multispectral X-ray imaging techniques for imaging gold nanorods *in vivo* as Part of predicting dose enhancing effects," in *Proc. IEEE Nucl. Sci. Symp., Med. Imag. Conf. Room-Temp. Semicond. Detect. Workshop (NSS/MIC/RTSD)*, Oct./Nov. 2016, pp. 1–2.
- [23] O. L. P. P. Scienti, J. C. Bamber, and D. Darambara, "Inclusion of a charge sharing correction algorithm into an X-ray photon counting spectral detector simulation framework," *IEEE Trans. Radiat. Plasma Med. Sci.*, early access, Jul. 13, 2020, doi: 10.1109/TRPMS.2020.3008861.
- [24] S. Jan, G. Santin, D. Strul, S. Staelens, K. Assie, D. Autret, S. Avner, R. Barbier, M. Bardies, P. M. Bloomfield, and D. Brasse, "GATE: A simulation toolkit for PET and SPECT," *Phys. Med. Biol.*, vol. 49, no. 19, pp. 4543–4561, 2004.
- [25] *COMSOL Multiphysics v5.2a*. Accessed: Sep. 2020. [Online]. Available: <http://www.comsol.com>
- [26] *Xcounter Actaeon Detector*. Accessed: Sep. 2020. [Online]. Available: <https://directconversion.com/product/xc-actaeon/>
- [27] T. H. Prettyman, "Method for mapping charge pulses in semiconductor radiation detectors," *Nucl. Instrum. Methods Phys. Res. A, Accel. Spectrom. Detect. Assoc. Equip.*, vol. 422, nos. 1–3, pp. 232–237, Feb. 1999.
- [28] M. E. Myronakis, M. Zvebil, and D. G. Darambara, "Computational modelling of pixelated CdZnTe detectors for X- and  $\gamma$ - ray imaging applications," *J. Instrum.*, vol. 7, no. 3, Mar. 2012, Art. no. P03004.



**OLIVER LEN PAUL PICKFORD SCIENTI** (Member, IEEE) was born in London, U.K., in 1988. He received the B.Sc. degree in Molecular Science and the B.Sc. degree in Natural Science (Biology) from The Open University, Milton Keynes, U.K., and the integrated M.Phys. degree from the University of Surrey, Guildford, U.K. This included a research placement at the National Physical Laboratory, Teddington, U.K. in 2014, analyzing the fission products of natU, after proton bombardment using gamma spectroscopy. He is currently pursuing the Ph.D. degree in physics and biomedical imaging with the Institute of Cancer Research, London, U.K.

He has been presenting regularly at the IEEE's Medical Imaging Conference since 2016 and the CERN's Medical Applications of Spectroscopic X-Ray Detectors' Closed Workshop since 2017. His current research interests include X-Ray photon counting spectral imaging, gamma spectroscopy,

photoacoustic spectral imaging, Monte Carlo modeling, and the use of gold nanoparticles for radiotherapy dose enhancement applications.

Mr. Pickford Scienti is also a member of the Institute of Physics, U.K., and was a recipient of the Christopher J. Thomson Best Student Paper Award from the IEEE Medical Imaging Conference in 2019.



**JEFFREY C. BAMBER** (Member, IEEE) received the B.Sc. degree in Physics from the University of Kent, Canterbury, U.K., in 1972, the M.Sc. degree in Biophysics and Bioengineering from the Chelsea College, University of London, U.K., in 1974, and the Ph.D. degree in Biophysics from the Institute of Cancer Research, University of London, U.K., in 1980.

He has been the Team Leader of Ultrasound and Optical Imaging since 1986, and is a Professor of Physics Applied to Medicine, the Deputy Dean (Biomedical Sciences) with the Institute of Cancer Research, and an Honorary Medical Physicist with the Royal Marsden Hospital, London. In 1993, he was a Guest Professor at the Tokyo Institute of Technology, Japan. From 1994 to 1995, he worked at the Medical Products Group, Hewlett-Packard, Andover, MA, USA. In 2017, he was a Gladden Short Stay Fellow of The University of Western Australia, Perth. He has authored 274 peer-reviewed articles, 16 book chapters, one book, and holds six patents. His inventions have become widely available on commercial ultrasound systems, and he serves as an advisor of several companies. His research interests include ultrasound imaging, speckle, clutter, elastography, contrast-enhanced imaging, photoacoustic imaging, quantitative biomarkers, functional and molecular imaging, cancer diagnosis, prognosis, response assessment, treatment guidance, and therapeutic delivery.

Prof. Bamber is the Vice-President of the IBUS Breast Imaging School, the past President of the International Association for Breast Ultrasound, and the past Vice-President of the International Society of Skin Imaging. He has received prizes, including 13 best paper/special status awards in peer-reviewed journals and two book publishing awards for excellence.



**DIMITRA G. DARAMBARA** (Member, IEEE) received the B.Sc. degree (Hons.) in Physics and Maths from the University of Athens, Greece, and the Ph.D. degree in physics from the University of Surrey, U.K.

She is currently a Senior Research Team Leader with the Institute of Cancer Research and Royal Marsden NHS Foundation Trust, London, U.K., where she established the Multimodality Molecular Imaging Translational Lab and Team since 2006. Previously, she was a Senior Research Fellow of the Yale, CERN, University College London, and the University of Surrey, always sponsored by prestigious personal research career development fellowships. Her Ph.D. degree was funded by the NATO on the development of a novel generic imaging detector, which was a breakthrough in semiconductor detector technology with a range of biomedical and industrial applications. Her research interests include conceptual design, the development and realization of emerging quantitative medical imaging techniques and innovative instrumentation, X-ray photon-counting and multi-spectral semiconductor detectors, and the combination of Monte Carlo and finite element analysis codes for advanced system performance optimization.

Dr. Darambara has been an active member of the Institute of Physics (Member, Chartered Physicist, and immediate past Chair of Medical Physics Group), the Institute of Physics and Engineering in Medicine, the European Society for Molecular Imaging and the IEEE (NPSS, EMBS, and WIE). She is also member of the Biomedical Engineering Board, Royal Academy of Engineering, U.K. Her IEEE related activities include serving as an Elected Member of the Nuclear Medical and Imaging Sciences Council (NMISC from 2017 to 2019), the IEEE Medical Imaging Conference Chair in 2019, and a Guest Editor of Thematic Special Issue on "Single Photon-Counting Spectral X-Ray CT Imaging" of the IEEE TRANSACTIONS ON RADIATION AND PLASMA MEDICAL SCIENCES. She was the recipient of the prestigious 2019 Phillips Award of the Institute of Physics for her significant contributions to physics and championing the Medical Physics discipline.

...